

Ground state properties and high pressure behavior of plutonium dioxide: Systematic density functional calculations

Ping Zhang,¹ Bao-Tian Wang,² and Xian-Geng Zhao¹

¹*LCP, Institute of Applied Physics and Computational Mathematics,*

Beijing 100088, People's Republic of China

²*Institute of Theoretical Physics and Department of Physics,*

Shanxi University, Taiyuan 030006, People's Republic of China

Abstract

Plutonium dioxide is of high technological importance in nuclear fuel cycle and is particularly crucial in long-term storage of Pu-based radioactive waste. Using first-principles density-functional theory, in this paper we systematically study the structural, electronic, mechanical, thermodynamic properties, and pressure induced structural transition of PuO₂. To properly describe the strong correlation in Pu 5*f* electrons, the local density approximation+*U* and the generalized gradient approximation+*U* theoretical formalisms have been employed. We optimize *U* parameter in calculating the total energy, lattice parameters, and bulk modulus at nonmagnetic, ferromagnetic, and antiferromagnetic configurations for both ground state fluorite structure and high pressure cotunnite structure. Best agreement with experiments is obtained by tuning the effective Hubbard parameter *U* at around 4 eV within LDA+*U* approach. After carefully testing the validity of the ground-state calculation, we further investigate the bonding nature, elastic constants, various moduli, Debye temperature, hardness, ideal tensile strength, and phonon dispersion for fluorite PuO₂. Some thermodynamic properties, e.g., Gibbs free energy, volume thermal expansion, and specific heat, are also calculated. As for cotunnite phase, besides elastic constants, various moduli, and Debye temperature at 0 GPa, we have further presented our calculated electronic, structural, and magnetic properties for PuO₂ under pressure up to 280 GPa. A metallic transition at around 133 GPa and an isostructural transition in pressure range of 75-133 GPa are predicted. Additionally, as an illustration on the valency trend and subsequent effect on the mechanical properties, the calculated results for other actinide metal dioxides (ThO₂, UO₂, and NpO₂) are also presented.

PACS numbers: 71.27.+a, 61.50.Ks, 62.20.-x, 63.20.dk

I. INTRODUCTION

Actinide elements and compounds possess particular interesting physical behaviors due to the $5f$ states and have always attracted extensive attention because of their importance in nuclear fuel cycle [1–4]. Actinide dioxides, AO_2 ($A=\text{Th, U, Np or Pu}$), are universally used as advanced fuel materials for nuclear reactors and PuO_2 also plays an important role in the plutonium re-use, separation and/or long-term storage. Recently, there has occurred in the literature a series of experimental reports [5–7] on the strategies of storage of Pu-based waste. Exposure to air and moisture, metallic plutonium surface easily oxidizes to Pu_2O_3 and PuO_2 . Although the existence of PuO_{2+x} ($x \leq 0.27$) was reported by Haschke *et al.* [5], recent photoemission study found that PuO_2 was only covered by a chemisorbed layer of oxygen and can be easily desorbed at elevated temperature [7], therefore, PuO_2 is the stablest plutonium oxide. At ambient condition PuO_2 crystallizes in a fluorite structure with space group $Fm\bar{3}m$ (No. 225). Its cubic unit cell is composed of four PuO_2 formula units with plutonium atoms and oxygen atoms in $4a$ and $8c$ sites, respectively. By using the energy dispersive x-ray diffraction method, Dancausse *et al* [8] reported that at 39 GPa, PuO_2 undergoes a phase transition to an orthorhombic structure of cotunnite type with space group $Pnma$ (No. 62).

As for the electronic-structure study of PuO_2 , conventional density functional theory (DFT) that applies the local density approximation (LDA) or generalized gradient approximation (GGA) underestimates the strong on-site Coulomb repulsion of the $5f$ electrons and, consequently, describes PuO_2 as incorrect ferromagnetic (FM) conductor [9] instead of antiferromagnetic (AFM) Mott insulator reported by experiment [10]. Same problems have been confirmed in studying other correlated materials within the pure LDA/GGA schemes. Fortunately, several approaches, the LDA/GGA+ U [11–13], the hybrid density functional of HSE [14], and the self-interaction corrected local spin-density (SIC-LSD) [15], have been developed to correct these failures in calculations of actinide compounds. The effective modification of pure DFT by LDA/GGA+ U formalisms has been confirmed widely in study of UO_2 [11, 13] and PuO_2 [16–20]. By tuning the effective Hubbard parameter in a reasonable range, the AFM Mott insulator feature was correctly calculated and the structural parameters as well as the electronic structure are well in accord with experiments. Lattice dynamical properties of UO_2 and PuO_2 and various contributions to their thermal conductivities were

studied by using a combination of LDA and Dynamical Mean-Field Theory (DMFT) [21]. However, despite that abundant researches on the structural, electronic, optical, thermodynamic properties of plutonium dioxide have been performed, relatively little is known regarding its chemical bonding, mechanical properties, and phonon dispersion. In addition, the pressure induced structural transition has also not yet been studied by first-principles DFT+ U calculations.

In this work, we have systematically calculated the ground-state structural parameters, electronic, mechanical, thermodynamic properties, and pressure induced structural transition of PuO₂ by employing the LDA+ U and GGA+ U schemes due to Dudarev *et al.* [11–13]. The validity of the ground-state calculation is carefully tested. Our calculated lattice parameter and bulk modulus B are well consistent with previous LDA+ U results [18]. The total energy, structural parameters, bulk modulus B , and pressure derivative of the bulk modulus B' for AFM and FM phases calculated in wide range of effective Hubbard U parameter are presented and our electronic spectrum reproduce briefly the main feature of our previous study [16]. In addition, the bonding nature of A–O bond in PuO₂, NpO₂, UO₂, and ThO₂ involving its mixed ionic/covalent character is investigated by performing the Bader analysis [22, 23]. We find that about 2.40, 2.48, 2.56, and 2.66 electrons transfer from each Pu, Np, U or Th atom to O atom, respectively. In study of the mechanical properties, we first calculate the elastic constants of both $Fm\bar{3}m$ and $Pnma$ phases and then the elastic moduli, Poisson’s ratio, and Debye temperature are deduced from the calculated elastic constants. Hardness and ideal tensile strength of $Fm\bar{3}m$ PuO₂ are also obtained by LDA+ U approach with one typical value of effective U parameter. The hardness of PuO₂ is equal to 26.6 GPa and the ideal tensile strengths are calculated to be 81.2, 28.3, and 16.8 GPa for pulling in the [001], [110], and [111] directions, respectively. As for the thermodynamic study, the phonon dispersion illustrates the stability of PuO₂ and we further predict the lattice vibration energy, thermal expansion, and specific heat by utilizing the quasiharmonic approximation based on the first-principles phonon density of state (DOS). One more aim of the present work is to extend the description of PuO₂ to high pressures. The electronic, structural, and magnetic behavior of PuO₂ under pressure up to 280 GPa have been evaluated. Results show that there occurs a metallic transition at around 133 GPa for $Pnma$ phase. The isostructural transition, similar to UO₂ [24] and ThO₂ [25], in pressure domain of 75-133 GPa is predicted. The rest of this paper is arranged as follows.

In Sec. II the computational method is briefly described. In Sec. III we present and discuss our results. In Sec. IV we summarize the conclusions of this work.

II. COMPUTATIONAL METHODS

The DFT calculations are performed on the basis of the frozen-core projected augmented wave (PAW) method of Blöchl [26] encoded in Vienna *ab initio* simulation package (VASP) [27] using the LDA and GGA [28, 29]. For the plane-wave set, a cutoff energy of 500 eV is used. The k -point meshes in the full wedge of the Brillouin zone (BZ) are sampled by $9 \times 9 \times 9$ and $9 \times 15 \times 9$ grids according to the Monkhorst-Pack [30] scheme for fluorite and cotunnite PuO_2 , respectively, and all atoms are fully relaxed until the Hellmann-Feynman forces become less than $0.02 \text{ eV}/\text{\AA}$. The plutonium $6s^2 7s^2 6p^6 6d^2 5f^4$ and the oxygen $2s^2 2p^4$ electrons are treated as valence electrons. The strong on-site Coulomb repulsion among the localized Pu $5f$ electrons is described by using the LDA/GGA+ U formalisms formulated by Dudarev *et al.* [11–13], where the double counting correction has already been included. As concluded in some previous studies of actinide dioxides (AO_2), although the pure LDA and GGA fail to depict the electronic structure, especially the insulating nature and the occupied-state character of UO_2 [24, 31], NpO_2 [18, 32], and PuO_2 [16, 17, 19], the LDA/GGA+ U approaches will capture the Mott insulating properties of the strongly correlated U $5f$, Np $5f$, and Pu $5f$ electrons in AO_2 adequately. In this paper the Coulomb U is treated as a variable, while the exchange energy is set to be a constant $J=0.75 \text{ eV}$. This value of J is same with our previous study of plutonium oxides [16, 17]. Since only the difference between U and J is significant [12], thus we will henceforth label them as one single parameter, for simplicity labeled as U , while keeping in mind that the non-zero J has been used during calculations.

Both spin-unpolarized and spin-polarized calculations are performed in this study. Compared to FM and AFM phases, the nonmagnetic (NM) phase is not energetically favorable both in the LDA+ U and GGA+ U formalisms. Therefore, the results of NM are not presented in the following. The dependence of the total energy (per formula unit at respective optimum geometries) on U for both FM and AFM phases within the LDA+ U and GGA+ U formalisms is shown in Fig. 1. At $U=0$ and 1.0 eV , the total energy of the FM phase is lower than that of the AFM phase either in LDA+ U scheme or GGA+ U scheme. However, as

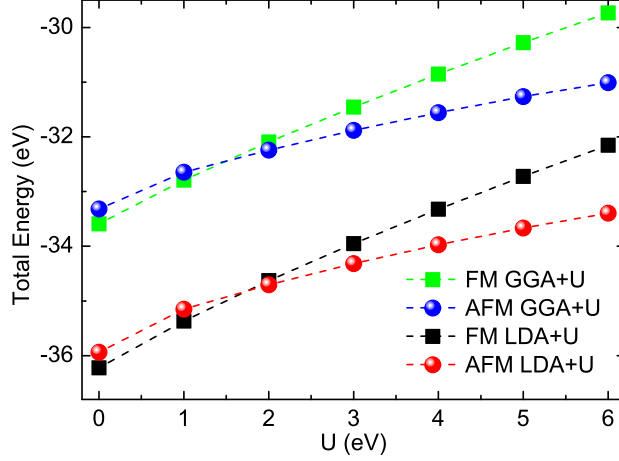


FIG. 1: (Color online) Dependence of the total energies (per formula unit) on U for FM and AFM PuO_2 .

shown in Fig. 1, it is clear that the total energy of the AFM phase decreases to become lower than that of the FM phase when increasing U . The total-energy differences ($E_{\text{FM}} - E_{\text{AFM}}$) within the LDA+ U and GGA+ U at $U=4$ eV are 0.705 and 0.651 eV, respectively. Both FM and AFM results will be presented in the following analysis. Besides, while the spin-orbit coupling (SOC) is important for certain properties of heavy metal compounds, it has been numerically found [9, 33] and physically analyzed [14, 34] that the inclusion of the SOC has little effect on the bulk and one-electron properties of UO_2 and PuO_2 . Our test calculations also show that within LDA+ U approach with $U=4$ eV, inclusion of SOC will increase the optimum lattice constant by only 0.7% and the bulk modulus by about 0.5 GPa. Therefore, in our following calculations of plutonium dioxide, the SOC is not included.

In present work, the theoretical equilibrium volume, bulk modulus B , and pressure derivative of the bulk modulus B' are obtained by fitting the energy-volume data with the third-order Birch-Murnaghan equation of state (EOS) [35]. In order to calculate elastic constants, a small strain is applied onto the structure. For small strain ϵ , Hooke's law is valid and the crystal energy $E(V, \epsilon)$ can be expanded as a Taylor series [36],

$$E(V, \epsilon) = E(V_0, 0) + V_0 \sum_{i=1}^6 \sigma_i \epsilon_i + \frac{V_0}{2} \sum_{i,j=1}^6 C_{ij} \epsilon_i \epsilon_j + O(\{\epsilon_i^3\}), \quad (1)$$

where $E(V_0, 0)$ is the energy of the unstrained system with the equilibrium volume V_0 , ϵ is

strain tensor which has matrix elements ε_{ij} ($i, j=1, 2, \text{ and } 3$) defined by

$$\varepsilon_{ij} = \begin{pmatrix} e_1 & \frac{1}{2}e_6 & \frac{1}{2}e_5 \\ \frac{1}{2}e_6 & e_2 & \frac{1}{2}e_4 \\ \frac{1}{2}e_5 & \frac{1}{2}e_4 & e_3 \end{pmatrix}, \quad (2)$$

and C_{ij} are the elastic constants. For cubic structures, there are three independent elastic constants (C_{11} , C_{12} , and C_{44}). So, the elastic constants for fluorite PuO_2 can be calculated from three different strains listed as follows:

$$\epsilon^1 = (\delta, \delta, \delta, 0, 0, 0), \epsilon^2 = (\delta, 0, \delta, 0, 0, 0), \epsilon^3 = (0, 0, 0, \delta, \delta, \delta). \quad (3)$$

The strain amplitude δ is varied in steps of 0.006 from $\delta=-0.036$ to 0.036 and the total energies $E(V, \delta)$ at these strain steps are calculated. After obtaining elastic constants, we can calculate bulk and shear moduli from the Voigt-Reuss-Hill (VRH) approximations [37]. The Voigt (Reuss) bounds on the bulk modulus B_V (B_R) and shear modulus G_V (G_R) for this cubic crystal system are deduced from the formulae of elastic moduli in Ref. [38]. As for cotunnite PuO_2 , the nine independent elastic constants (C_{11} , C_{12} , C_{13} , C_{22} , C_{23} , C_{33} , C_{44} , C_{55} , and C_{66}) can be obtained from nine different strains listed in the following:

$$\begin{aligned} \epsilon^1 &= (\delta, 0, 0, 0, 0, 0), \epsilon^2 = (0, \delta, 0, 0, 0, 0), \epsilon^3 = (0, 0, \delta, 0, 0, 0), \\ \epsilon^4 &= (0, 0, 0, \delta, 0, 0), \epsilon^5 = (0, 0, 0, 0, \delta, 0), \epsilon^6 = (0, 0, 0, 0, 0, \delta), \\ \epsilon^7 &= (\delta, \delta, 0, 0, 0, 0), \epsilon^8 = (0, \delta, \delta, 0, 0, 0), \epsilon^9 = (\delta, 0, \delta, 0, 0, 0) \end{aligned} \quad (4)$$

and the formulae of elastic moduli in VRH approximations [37] are from Ref. [39]. Based on the Hill approximation [37], $B=\frac{1}{2}(B_R + B_V)$ and $G=\frac{1}{2}(G_R + G_V)$. The Young's modulus E and Poisson's ratio ν are given by the following formulae:

$$E = 9BG/(3B + G), \nu = (3B - 2G)/[2(3B + G)]. \quad (5)$$

In addition, the elastic properties of a solid can also be related to thermodynamical parameters especially specific heat, thermal expansion, Debye temperature, melting point, and Grüneisen parameter [40]. From this point of view, Debye temperature is one of fundamental parameters for solid materials. Due to the fact that at low temperatures the vibrational excitations arise solely from acoustic vibrations, therefore, the Debye temperature calculated

from elastic constants is the same as that determined from specific heat measurements. The relation between the Debye temperature (θ_D) and the average sound wave velocity (v_m) is

$$\theta_D = \frac{h}{k_B} \left(\frac{3n}{4\pi\Omega} \right)^{1/3} v_m, \quad (6)$$

where h and k_B are Planck and Boltzmann constants, respectively, n is the number of atoms in the molecule and Ω is molecular volume. The average wave velocity in the polycrystalline materials is approximately given as

$$v_m = \left[\frac{1}{3} \left(\frac{2}{v_t^3} + \frac{1}{v_l^3} \right) \right]^{-1/3}, \quad (7)$$

where $v_t = \sqrt{G/\rho}$ (ρ is the density) and $v_l = \sqrt{(3B + 4G)/3\rho}$ are the transverse and longitudinal elastic wave velocities of the polycrystalline materials, respectively.

III. RESULTS

A. Atomic and electronic structures of fluorite PuO₂

We report in Table I the lattice parameter (a_0), bulk modulus (B), and pressure derivative of the bulk modulus (B') for AFM and FM PuO₂ obtained in LDA+ U and GGA+ U frameworks. All these values are determined by EOS fitting. For comparison, the experimental values of a_0 (Ref. [5]) and B (Ref. [41]) are also listed. In the overall view, the dependence of the lattice parameter a_0 of AFM PuO₂ on U is well consistent with our previous study [16] either in LDA+ U scheme or in GGA+ U scheme. For the LDA/GGA+ U approaches, the calculated a_0 improves upon the pure LDA/GGA by steadily increasing its amplitude with U . Actually, at a typical value $U=4$ eV, the LDA+ U gives $a_0=5.362$ Å, which is very close to the experimental value of 5.398 Å, and the GGA+ U gives $a_0=5.466$ Å. Note that recent PBE+ U [19] and LDA+ U [18] calculations with $U=4.0$ eV and $J=0.7$ eV predicted the lattice parameter of AFM PuO₂ to be 5.444 and 5.354 Å, respectively, and the HSE [14] and SIC-LSD [15] calculations gave the values to be 5.385 and 5.44 Å, respectively. On the other hand, as shown in Table I, the tendency of a_0 with U for FM PuO₂ is similar to that of the AFM phase. At a typical value $U=4$ eV, the LDA/GGA+ U give $a_0=5.338$ and 5.452 Å. These values are slightly smaller than those of the AFM phase. Previous HSE [14] calculation of FM PuO₂ gave the lattice parameter to be 5.387 Å. As for the dependence of

TABLE I: Calculated lattice parameters (a_0), bulk modulus (B), and pressure derivative of the bulk modulus (B') for AFM and FM PuO₂ at 0 GPa. For comparison, experimental values are also listed.

Magnetism	Method	property	$U=0$	$U=1$	$U=2$	$U=3$	$U=4$	$U=5$	$U=6$	Expt.	
AFM	LDA+ U	a_0 (Å)	5.275	5.313	5.338	5.351	5.362	5.371	5.378	5.398 ^a	
		B (GPa)	218	208	224	224	225	226	227	178 ^b	
		B'	4.1	3.7	4.3	4.3	4.3	4.3	4.3		
	GGA+ U	a_0 (Å)	5.396	5.433	5.446	5.457	5.466	5.473	5.480		
		B (GPa)	185	188	191	192	193	194	195		
		B'	4.3	3.8	4.4	4.5	4.5	4.5	4.4		
	FM	LDA+ U	a_0 (Å)	5.270	5.290	5.309	5.325	5.338	5.350	5.361	
			B (GPa)	230	224	221	220	218	215	212	
			B'	4.4	4.4	4.3	4.4	4.4	4.4	4.5	
GGA+ U		a_0 (Å)	5.384	5.405	5.424	5.439	5.452	5.464	5.476		
		B (GPa)	193	188	186	184	182	179	174		
		B'	4.5	4.4	4.5	4.5	4.7	4.7	4.8		

^a Reference [5], ^b Reference [41].

bulk modulus B of AFM and FM PuO₂ on U , it is clear that the LDA results are always higher than the GGA results, which is due to the overbinding effect of the LDA approach. While the bulk modulus B of AFM phase increases steadily with increasing the amplitude of U , the bulk modulus B of FM phase will decrease along with the increasing of Hubbard U . At a typical value $U=4$ eV, the LDA+ U and GGA+ U give $B=225$ and 193 GPa for AFM phase, respectively, and $B=218$ and 182 GPa for FM phase, respectively. Apparently, the GGA+ U approach gives more close values to the experimental data of $B=178$ GPa [41]. In our present study, as shown in Table II, the bulk modulus B deduced from elastic constants turns out to be very close to that obtained by EOS fitting. This indicates that our calculations are consistent and reliable. In addition, as listed in Table II, recent PBE+ U [19] and LDA+ U [18] calculations with $U=4.0$ eV and $J=0.7$ eV predicted the bulk modulus B of AFM PuO₂ to be 199 and 226 GPa, respectively, and the HSE [14] and SIC-LSD [15] calculations gave the the bulk modulus to be 221 and 214 GPa, respectively. As for pressure

TABLE II: Calculated elastic constants, various moduli, Poisson’s ratio (ν), spin moments ($\mu_{mag.}$), and energy band gap (E_g) for $Fm\bar{3}m$ AFM PuO₂ at 0 GPa. For comparison, experimental values and other theoretical results are also listed.

Method	C_{11}	C_{12}	C_{44}	B	G	E	ν	$\mu_{mag.}$	E_g
	(GPa)	(GPa)	(GPa)	(GPa)	(GPa)	(GPa)		(μ_B)	(eV)
LDA+ U ($U=0$)	386.6	136.5	71.9	220	89.9	237.3	0.320	3.937	0.0
LDA+ U ($U=4$)	319.6	177.8	74.5	225	73.0	197.7	0.354	4.126	1.5
GGA+ U ($U=0$)	343.9	112.3	53.7	190	73.5	195.1	0.328	4.085	0.0
GGA+ U ($U=4$)	256.5	167.9	59.2	197	52.7	145.2	0.377	4.165	1.5
Expt.				178 ^a					1.8 ^b
PBE+ U^c				199				3.89	2.2
LDA+ U^d				226					1.7
HSE ^e				221					3.4
SIC-LSD ^f				214					1.2

^a Reference [41], ^b Reference [10], ^c Reference [19], ^d Reference [18], ^e Reference [14], ^f Reference [15].

derivative of the bulk modulus (B'), all our calculated values are approximately equal to 4.5. Overall, comparing with the experimental data and recent theoretical results, the accuracy of our atomic-structure prediction for AFM PuO₂ is quite satisfactory by tuning the effective Hubbard parameter U in a range of 3-4 eV within the LDA/GGA+ U approaches, which supplies the safeguard for our following study of electronic structure and mechanical properties of PuO₂.

The total density of states (DOS) as well as the projected DOS for the Pu 5*f* and O 2*p* orbitals within LDA, GGA, LDA+ U , and GGA+ U formalisms are shown in Fig. 2. Clearly, our results reproduce all the features included in our previous work [16]. In particular, we recover the main conclusion that although the pure LDA and GGA fail to depict the electronic structure, especially the insulating nature and the occupied-state character of PuO₂, by tuning the effective Hubbard parameter in a reasonable range, the LDA/GGA+ U approaches can prominently improve upon the pure LDA/GGA calculations and, thus, can provide a satisfactory qualitative electronic structure description comparable with the pho-

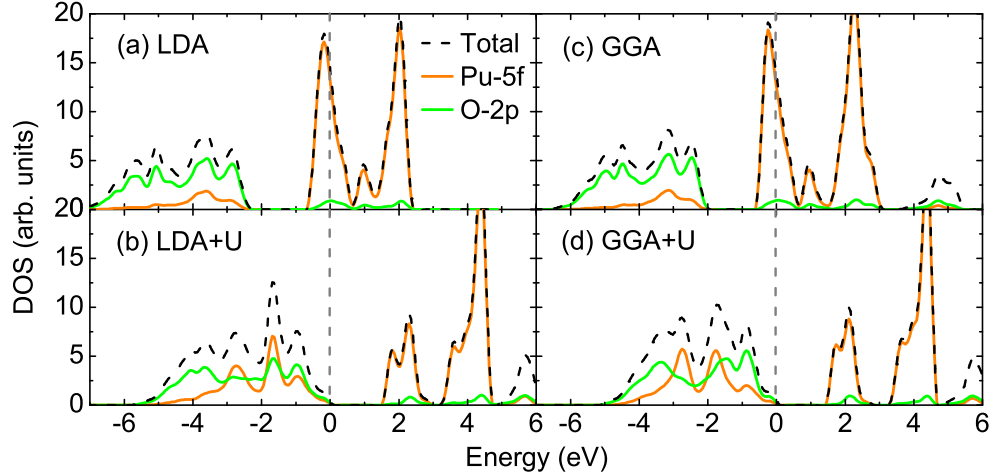


FIG. 2: (Color online) The total DOS for the PuO_2 AFM phase computed in the (a) LDA, (b) LDA+ U ($U=4$), (c) GGA, and (d) GGA+ U ($U=4$) formalisms. The projected DOSs for the Pu 5 f and O 2 p orbitals are also shown. The Fermi energy level is set at zero.

toemission experiments [6, 7]. In this study, the insulating energy band gap (E_g) is of 1.5 eV at $U=4$ eV within LDA/GGA+ U approaches (see Table II). In Table II, the experimental [10] value and previous theoretical calculations [14, 15, 18, 19] results are also listed for comparison. Obviously, the HSE calculations result in a larger E_g by ~ 1.9 eV [14] and our calculated results are well consistent with the measured value and other theoretical results. The calculated amplitude of local spin moment is $\sim 4.1 \mu_B$ (per Pu atom) for AFM PuO_2 within the two DFT+ U schemes and this value is comparable to previous LDA/PBE+ U [19] results of $\sim 3.9 \mu_B$.

To understand the chemical bonding characters of fluorite PuO_2 , we present in Fig. 3 the crystal structure of its cubic unit cell and the charge density map of the (110) plane calculated in LDA+ U formalism with $U=4$ eV for AFM phase. Evidently, the charge density around Pu and O ions are all near spherical distribution with slightly deformed toward the direction to their nearest neighboring atoms and there are clear covalent bridges between Pu and O ions. In order to describe the ionic/covalent character quantitatively and more clearly, we plot the line charge density distribution along the nearest Pu–O bonds (not shown). A minimum value of charge density ($0.53 e/\text{\AA}^3$) along the Pu–O bonds is obtained and is listed in Table III. For comparison, we have also calculated some corresponding properties of AFM UO_2 within the LDA+ U formalism. Parameters of the Hubbard term are taken as

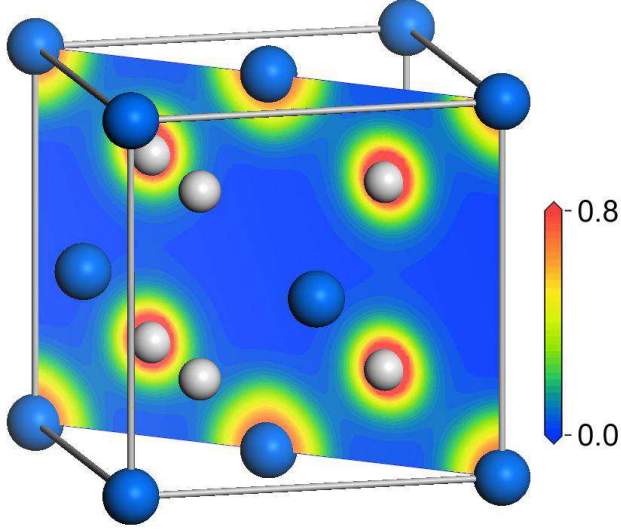


FIG. 3: (Color online) Cubic unit cell for PuO_2 in space group $Fm\bar{3}m$. The larger blue spheres represent plutonium atoms and the smaller white O atoms. A slice of the isosurfaces of the electron density for AFM phase in (110) plane calculated in the LDA+ U formalisms with $U=4$ eV is also presented (in unit of $e/\text{\AA}^3$)

TABLE III: Calculated charge and volumes according to Bader partitioning as well as the $A-O$ distances and correlated minimum values of charge density along the $A-O$ bonds for actinide dioxides.

Compound	$Q_B(A)$	$Q_B(O)$	$V_B(A)$	$V_B(O)$	$A-O$	Charge density _{min.}
	(e)	(e)	(\AA^3)	(\AA^3)	(\AA)	($e/\text{\AA}^3$)
PuO_2	13.60	7.20	15.36	11.58	2.32	0.53
NpO_2	12.52	7.24	15.69	11.83	2.34 ^a	0.51 ^a
UO_2	11.44	7.28	16.35	12.05	2.36	0.52
ThO_2	9.34	7.33	17.67	13.35	2.43 ^b	0.45 ^b

^a Reference [32], ^b Reference [25].

$U=4.51$ eV and $J=0.51$ eV, which had been checked carefully by Dudarev *et al* [11–13]. In following study, results of UO_2 are all calculated using these Hubbard parameters either for ground-state $Fm\bar{3}m$ phase or high pressure $Pnma$ phase. The lattice parameter $a_0=5.449$ \AA and bulk modulus $B=220.0$ GPa for $Fm\bar{3}m$ UO_2 obtained by EOS fitting are in perfect agreement with results of recent LDA+ U calculation [18] ($a_0=5.448$ \AA and $B=218$ GPa)

and experiments [41, 52] ($a_0=5.47 \text{ \AA}$ and $B=207 \text{ GPa}$). Charge analysis results of $Fm\bar{3}m$ UO_2 are listed in Table III. Clearly, the minimum values of charge density for PuO_2 and UO_2 , comparable to that along the Np-O bonds included in our previous study of NpO_2 [32], are prominently larger than that along the Th-O bonds (0.45 e/\AA^3) in ThO_2 [25]. This indicates that the Pu-O , U-O , and Np-O bonds have stronger covalency than the Th-O bonds. And this conclusion is in good accordance with previous HSE study of the covalency in Ref. [2], in which significant orbital mixing and covalency in the intermediate region ($\text{PuO}_2\text{-CmO}_2$) of actinide dioxides was for the first time showed by the increasing $5f\text{-}2p$ orbital energy degeneracy. Besides, the $A\text{-O}$ ($A=\text{Pu, Np, U or Th}$) bond distances calculated in present study and our previous works [25, 32] are listed in Table III. Obviously, the Pu-O , Np-O , and U-O bond distances are all smaller than the Th-O bond distance. This fact illustrates that the covalency of AO_2 has tight relation with their bond distances, thus influences their macroscopical properties, such as hardness and elasticity. To see the ionicity of AO_2 , results from the Bader analysis [22, 23] are presented in Table III. The charge (Q_B) enclosed within the Bader volume (V_B) is a good approximation to the total electronic charge of an atom. Note that although we have included the core charge in charge density calculations, since we do not expect variations as far as the trends are concerned, only the valence charge are listed. Here, same with our previous study, we apply $U=4.6 \text{ eV}$ and $J=0.6 \text{ eV}$ for the $\text{Np } 5f$ orbitals in calculations of NpO_2 . Based on the data in Table III and considering the valence electron numbers of Pu , Np , U , Th , and O atoms (16, 15, 14, 12, and 6, respectively), in our study of AO_2 , we find that about 2.40, 2.48, 2.56, and 2.66 electrons transfer from each Pu , Np , U or Th atom to O atom, respectively. This indicates that the ionicity of AO_2 shows decreasing trend with increasing Z .

B. Mechanical properties

1. Elastic properties

Our calculated elastic constants, various moduli, and Poisson's ratio ν of the $Fm\bar{3}m$ PuO_2 at 0 GPa are collected in Table II and those of the $Pnma$ phase are listed in Table IV. Obviously, the $Fm\bar{3}m$ phase of PuO_2 is mechanically stable due to the fact that its elastic

TABLE IV: Calculated elastic constants, elastic moduli, pressure derivative of the bulk modulus B' , and Poisson's ratio ν for cotunnite-type PuO_2 and UO_2 at 0 GPa. Except B' and ν , all other values are in units of GPa.

Compound	C_{11}	C_{22}	C_{33}	C_{44}	C_{55}	C_{66}	C_{12}	C_{23}	C_{13}	B	B'	B_a	B_b	B_c	G	E	ν
PuO_2	355.6	327.4	336.3	36.0	81.5	96.7	140.5	199.0	141.2	219.9	5.7	598.5	669.5	720.3	73.0	197.2	0.351
UO_2	338.2	335.1	325.9	24.4	75.6	92.0	119.9	148.4	142.1	202.2	5.5	586.4	593.8	641.9	68.0	183.4	0.349

constants satisfy the following mechanical stability criteria [36] of cubic structure:

$$C_{11} > 0, C_{44} > 0, C_{11} > |C_{12}|, (C_{11} + 2C_{12}) > 0. \quad (8)$$

As for the high-pressure $Pnma$ crystalline phase, we have optimized the structural parameters of its AFM phase at different pressures within LDA+ U formalism with the typical value of $U=4$ eV. To avoid the Pulay stress problem, we perform the structure relaxation calculations at fixed volumes rather than constant pressures. Note that different from the structure optimization of the ground-state $Fm\bar{3}m$ phase, the coordinates of atoms and the cell shape of the $Pnma$ phase are necessary to be optimized due to its internal degrees of freedom. After fitting the energy-volume data to the EOS, we obtain the optimized structural lattice parameters a , b , and c for the $Pnma$ PuO_2 AFM phase at 0 GPa to be 5.889, 3.562, and 6.821 Å, respectively, giving $V=143.1$ Å³. This volume is smaller than the equilibrium volume of 154.2 Å³ for the $Fm\bar{3}m$ phase. This feature implies that the $Pnma$ phase will become stable under compression. The elastic constants listed in Table IV indicate that the $Pnma$ PuO_2 is also mechanically stable. Actually, they satisfy the following mechanical stability criteria [36] for the orthorhombic structure:

$$\begin{aligned} C_{11} > 0, C_{22} > 0, C_{33} > 0, C_{44} > 0, C_{55} > 0, C_{66} > 0, \\ [C_{11} + C_{22} + C_{33} + 2(C_{12} + C_{13} + C_{23})] > 0, \\ (C_{11} + C_{22} - 2C_{12}) > 0, (C_{11} + C_{33} - 2C_{13}) > 0, \\ (C_{22} + C_{33} - 2C_{23}) > 0. \end{aligned} \quad (9)$$

One can see from Table IV that the calculated C_{12} , C_{23} , and C_{13} are largely smaller than C_{11} , C_{22} , and C_{33} . Therefore, the mechanical stability criteria is easily satisfied. For comparison, we have also calculated the elastic properties of UO_2 in its ground-state fluorite phase and

high-pressure cotunnite phase within LDA+ U formalism. For $Fm\bar{3}m$ phase, $C_{11}=389.3$ GPa, $C_{12}=138.9$ GPa, $C_{44}=71.3$ GPa, $B=222.4$ GPa, $G=89.5$ GPa, $E=236.8$ GPa, and Poisson's ratio $\nu=0.323$. Results for $Pnma$ UO_2 are presented in Table IV. Clearly, both fluorite and cotunnite phases of UO_2 are mechanically stable. Moreover, comparing results of bulk modulus B , shear modulus G , Young's modulus E , and Poisson's ratio ν for fluorite phase and cotunnite phase, they are almost equal to each other for PuO_2 . Particularly, the bulk modulus B is only smaller by about 5 GPa for $Pnma$ phase compared to that of $Fm\bar{3}m$ phase. As for UO_2 , bulk modulus of cotunnite phase is smaller by approximately 9%, shear modulus and Young's modulus about 23%, compared to those of fluorite structure. Besides, in our previous study of ThO_2 [25] we find that the bulk modulus, shear modulus, and Young's modulus of cotunnite ThO_2 are all smaller by approximately 25% compared to those of fluorite ThO_2 . Therefore, after comparing the bulk modulus B for the two phases of ThO_2 , UO_2 , and PuO_2 , we find that the difference is decreasing along with increasing of 5*f* electrons. This trend is understandable. Although the softening in bulk modulus upon phase transition for these three systems is similar, the increase of 5*f* electrons of actinide metal atoms will lead to more covalency and thus reduce the bulk modulus difference between the two phases of the actinide dioxides across the series. To study the anisotropy of the linear bulk modulus for $Pnma$ PuO_2 and UO_2 , we calculate the directional bulk modulus along the **a**, **b** and **c** axis by the following equations [40],

$$B_a = \frac{\Lambda}{1 + \alpha + \beta}, B_b = \frac{B_a}{\alpha}, B_c = \frac{B_a}{\beta}, \quad (10)$$

where $\Lambda=C_{11}+2C_{12}\alpha+C_{22}\alpha^2+2C_{13}\beta+C_{33}\beta^2+2C_{23}\alpha\beta$. For orthorhombic crystals,

$$\alpha = \frac{(C_{11} - C_{12})(C_{33} - C_{13}) - (C_{23} - C_{13})(C_{11} - C_{13})}{(C_{33} - C_{13})(C_{22} - C_{12}) - (C_{13} - C_{23})(C_{12} - C_{23})} \quad (11)$$

and

$$\beta = \frac{(C_{22} - C_{12})(C_{11} - C_{13}) - (C_{11} - C_{12})(C_{23} - C_{12})}{(C_{22} - C_{12})(C_{33} - C_{12}) - (C_{12} - C_{23})(C_{13} - C_{23})} \quad (12)$$

are defined as the relative change of the **b** and **c** axis as a function of the deformation of the **a** axis. After calculation, we obtain values of α and β to be 0.8939 (0.9875) and 0.8309 (0.9135) for PuO_2 (UO_2), respectively. Results of B_a , B_b , and B_c are presented in Table IV. Clearly, results of the directional bulk moduli show that both $Pnma$ PuO_2 and UO_2 are easily compressed along **a** axis at 0 GPa. The longest axis **c** is the hardest axis for these two

TABLE V: Calculated density (in g/cm^3), transverse (v_t), longitudinal (v_l) and average (v_m) sound velocities (in m/s) derived from bulk and shear modulus, and Debye temperature (in K) for actinide dioxides. Results of NpO_2 and ThO_2 are calculated by using the elastic data included in our previous studies [25, 32].

Compound	Phase	ρ	v_t	v_l	v_m	θ_D
PuO_2	$Fm\bar{3}m$	11.892	2477.6	5206.3	2787.0	354.5
PuO_2	$Pnma$	12.812	2387.0	4976.0	2683.9	350.0
NpO_2	$Fm\bar{3}m$	11.347	2835.0	5566.5	3176.8	401.2
UO_2	$Fm\bar{3}m$	11.084	2841.8	5552.7	3183.4	398.1
UO_2	$Pnma$	11.957	2384.2	4948.5	2680.2	343.7
ThO_2	$Fm\bar{3}m$	9.880	2969.1	5575.5	3317.3	402.6
ThO_2	$Pnma$	10.505	2504.6	4738.4	2799.8	346.8

actinide dioxides. Directional bulk moduli of PuO_2 are all bigger than the corresponding values of UO_2 . Moreover, using results of elastic constants included in previous study [25], the directional bulk moduli B_a , B_b , and B_c of $Pnma$ ThO_2 are calculated to be 528.3, 406.3, and 415.8 GPa, respectively. This illustrates that, in contrary to $Pnma$ PuO_2 and UO_2 , the $Pnma$ ThO_2 is relatively harder to be compressed along \mathbf{a} axis compared to other two axes. And all three directional bulk moduli of $Pnma$ ThO_2 are apparently smaller than that of $Pnma$ PuO_2 and UO_2 , which indicates relative weaker covalency of ThO_2 compared with PuO_2 and UO_2 in their high pressure phase.

2. Debye temperature

In study of the sound velocities and Debye temperature, our calculated results of AFM PuO_2 and AFM UO_2 in their fluorite phase and high pressure cotunnite phase are presented in Table V. For comparison, results of NpO_2 and ThO_2 calculated by using the elastic data included in our previous studies [25, 32] are also listed. As seen from Table V, in their $Fm\bar{3}m$ structure, Debye temperature and sound velocity of UO_2 , NpO_2 , and ThO_2 are higher than that of PuO_2 . This is interestingly associated with the fact that Debye temperature (θ_D)

and Vickers hardness (H) of materials follow an empirical relationship [42]:

$$\theta_D \propto H^{1/2} \Omega^{1/6} M^{-1/2}, \quad (13)$$

where M is molar mass and Ω is molecular volume. Although $Fm\bar{3}m$ PuO_2 has close value of hardness compared with UO_2 and NpO_2 , it has relatively smaller molecular volume and larger molar mass, as a consequence, has a lower Debye temperature than that of UO_2 and NpO_2 . As for the $Pnma$ structure, Debye temperature and sound velocity of PuO_2 , UO_2 , and ThO_2 are lower than those of their $Fm\bar{3}m$ structure. This is since that the $Pnma$ PuO_2 , UO_2 , and ThO_2 have smaller values of volume, bulk and shear moduli compared to their ground-state $Fm\bar{3}m$ structure.

3. Hardness

Hardness is also one fundamental physical quantity when considering the phase stability and mechanical properties. According to the hardness conditions [43], the hardness is closely related to interatomic distances, number of nearest neighbors, directional bonding, anisotropy, and the indenter orientation in the structures. To date there is still no available calculation method involving hardness anisotropy in different dimensions in the literature. In spite of that, however, recently a semiempirical approach of hardness was raised by Simunek and Vackar [44, 45] in terms of the atomistic bond strength properties. This approach has been successfully tested by the authors on the more than 30 binary structures with zinc blende, cubic fluorite, rock salt crystals, and also for highly covalent crystals [44, 45]. There is no need for all those high-symmetry structures to consider the anisotropy. Also, this method has been applied to the crystals involving covalent and ionic bonding characters, such as in the compounds of transition metal and light atoms, and generalized to the complex structure with more than two different bond strengths [44, 45]. Moreover, in study of covalent crystals, the results of the method raised by Simunek and Vackar [44, 45] agree well with those of another hardness method of Gao and co-workers [46]. Therefore, the hardness of optimized cubic fluorite structures of actinide dioxides can be calculated by the method of Simunek and Vackar [44, 45]. In the case of two atoms 1 and 2 forming one bond of strength s_{12} in a unit cell of volume Ω , the expression for hardness has the form [44]

$$H = (C/\Omega)b_{12}s_{12}e^{-\sigma f_2}, \quad (14)$$

where

$$s_{12} = \sqrt{(e_1 e_2)} / (n_1 n_2 d_{12}), e_i = Z_i / r_i \quad (15)$$

and

$$f_2 = \left(\frac{e_1 - e_2}{e_1 + e_2} \right)^2 = 1 - [\sqrt{(e_1 e_2)} / (e_1 + e_2)]^2 \quad (16)$$

are the strength and ionicity of the chemical bond, respectively, and d_{12} is the interatomic distance; $C=1550$ and $\sigma=4$ are constants. The radius r_i is chosen to make sure that the sphere centered at atoms i in a crystal contains exactly the valence electronic charge Z_i . For fluorite structure PuO_2 , $b_{12}=32$ counts the interatomic bonds between atoms Pu (1) and O (2) in the unit cell, $n_1=8$ and $n_2=4$ are coordination numbers of atom Pu and O, respectively, $r_1=1.698$ (Å) and $r_2=1.005$ (Å) are the atomic radii for Pu and O atoms, respectively, $Z_1=16$ and $Z_2=6$ are valence charge for Pu and O atoms, respectively, $d_{12}=2.32$ (Å) is the interatomic distance, and $\Omega=154.16$ (Å³) is the volume of unit cell. As for fluorite UO_2 , $b_{12}=32$, $n_1=8$, $n_2=4$, $r_1=1.737$ (Å), $r_2=1.003$ (Å), $Z_1=14$, $Z_2=6$, $d_{12}=2.36$ (Å), $\Omega=161.82$ (Å³). Using Eqs. (14)-(16), we obtain $s_{12}=0.1010$ and $f_2=0.0503$ for PuO_2 and $s_{12}=0.0919$ and $f_2=0.0219$ for UO_2 . Therefore, the hardness of PuO_2 at its ground-state fluorite structure can be described as $H=26.6$ (GPa) and for UO_2 $H=25.8$ (GPa). Clearly, the hardness of PuO_2 , almost equal to the hardness of NpO_2 (26.5 GPa) [32], is slightly larger than that of UO_2 . Besides, these three values of hardness are all larger than that of ThO_2 (22.4 GPa) [25].

4. Theoretical tensile strength

Although many efforts have been paid on PuO_2 , little is known on its theoretical tensile strength. The ideal strength of materials is the stress that is required to force deformation or fracture at the elastic instability. Although the strength of a real crystal can be changed by the existing cracks, dislocations, grain boundaries, and other microstructural features, its theoretical value can never be raised, i.e., the theoretical strength sets an upper bound on the attainable stress. Here, we employ a first-principles computational tensile test (FPCTT) [47] to calculate the stress-strain relationship and obtain the ideal tensile strength by deforming the PuO_2 crystals to failure. The anisotropy of the tensile strength is tested by pulling the initial fluorite structure along the [001], [110], and [111] directions. As shown in Fig. 4, three geometric structures are constructed to investigate the tensile strengths in the three

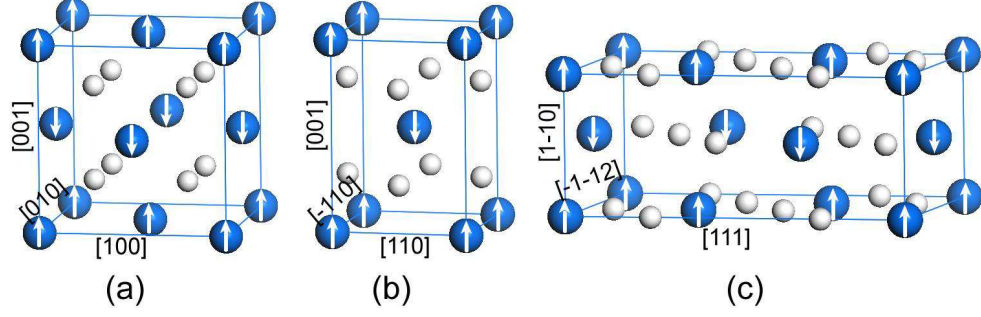


FIG. 4: (Color online) Schematic illustration of tension along (a) [001], (b) [110], and (c) [111] orientations. The AFM order is indicated by white arrows attached on Pu atoms.

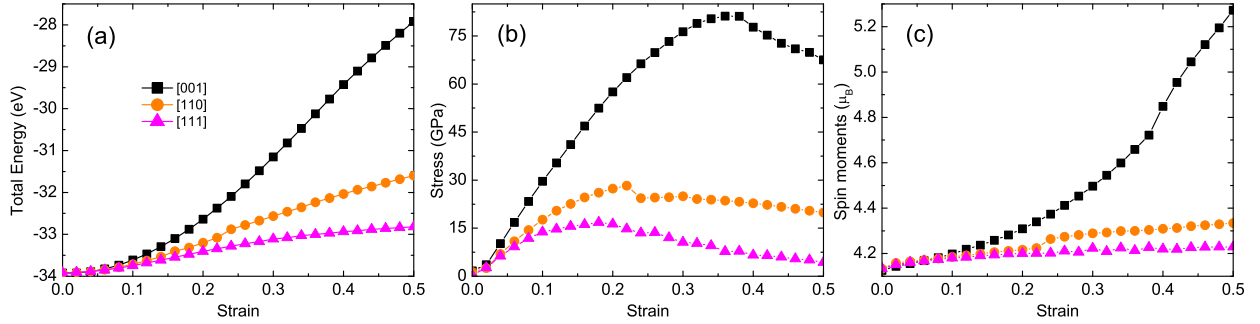


FIG. 5: (Color online) Dependence of the (a) total energy (per formula unit), (b) stress, and (c) spin moments on tensile strain for AFM PuO_2 in the [001], [110], and [111] directions.

typical crystallographic directions: 4(a) shows a general fluorite structure of PuO_2 with four Pu and eight O atoms; 4(b) a body-centered tetragonal (bct) unit cell with two Pu and four O; and 4(c) a orthorhombic unit cell with six Pu and twelve O. In FPCTT, the tensile stress is calculated according to the Nielsen-Martin scheme [48] $\sigma_{\alpha\beta} = \frac{1}{\Omega} \frac{\partial E_{\text{total}}}{\partial \varepsilon_{\alpha\beta}}$ where $\varepsilon_{\alpha\beta}$ is the strain tensor ($\alpha, \beta=1,2,3$) and Ω is the volume at the given tensile strain. Tensile process along the [001], [110], and [111] directions is implemented by increasing the lattice constants along these three orientations step by step. At each step, the structure is fully relaxed until all other five stress components vanished except that in the tensile direction.

The calculated total energy, stress, and spin moments as functions of uniaxial tensile strain for AFM PuO_2 in the [001], [110], and [111] directions are shown in Fig. 5. Clearly, all three energy-strain curves increase with increasing tensile strain, but one can easily find the inflexions by performing differentiations. Actually, at strains of 0.36, 0.22, and 0.18,

TABLE VI: Calculated stress maxima and the corresponding strains in the tensile process.

Direction	Stress (GPa)	Strain
[001]	81.2	0.36
[110]	28.3	0.22
[111]	16.8	0.18

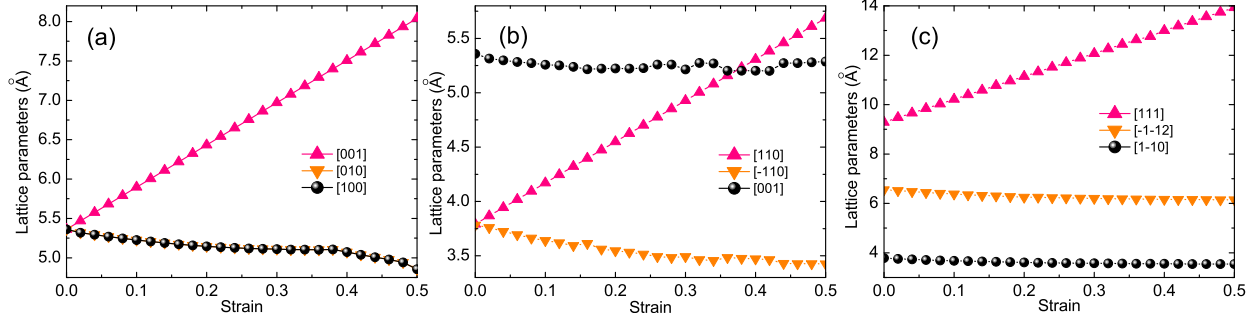


FIG. 6: (Color online) Dependence of the lattice parameters on tensile strain for AFM PuO_2 in the (a) [001], (b) [110], and (c) [111] directions.

the stresses reach maxima 81.2, 28.3, and 16.8 GPa for pulling in the [001], [110], and [111] directions, respectively. For clear comparison, all these maximum stresses (i.e., the theoretical tensile strengths in the three typical crystalline orientations) and the corresponding strains are listed in Table VI. Our results indicate that the [001] direction is the strongest tensile direction and [111] the weakest. In fact, there are eight Pu–O bonds per formula unit for fluorite PuO_2 . The angle of all eight bonds with respect to the pulling direction is 45° in [001] direction. However, in [110] direction only four bonds make an angle of 45° with the pulling direction. Four other bonds are vertical to the pulling direction. In [111] direction, two bonds are parallel to the pulling direction and six others make an angle of about 19.5° with the pulling direction. The bonds vertical to the pulling direction have no contributions on the tensile strength and the bonds parallel to the pulling direction are easy to fracture under tensile deformation. Therefore, the fact that the tensile strength along the [001] direction is stronger than that along other two directions is understandable. Besides, we note that the stress in [110] direction experiences an abrupt decrease process after strain up to 0.24. This is due to the fact that the corresponding four Pu–O bonds

(make an angle of 45° with the pulling direction) have been pulled to fracture. The fracture behaviors have been clarified by plotting valence electron charge density maps (not shown). Under the same strain, the abrupt increase of spin moment can be clearly seen [Fig. 5(c)]. While the spin moments in [110] and [111] directions only increase from 4.13 to 4.23 and $4.33 \mu_B$, respectively, the spin moments in [001] direction increase up to $5.27 \mu_B$ at the end of tensile deformation. In addition, the evolutions of the lattice parameters with strain in all three tensile processes are presented in Fig. 6. One can see from Fig. 6 that along with the increase of the lattice parameter in the pulling direction, other two lattice parameters vertical to the pulling direction are decrease smoothly. In [001] direction, the evolutions of the lattice parameters along [100] and [010] directions are absolutely same due to the structural symmetry. For all three tensile deformations, no structural transition has been observed in our present FPCTT study.

C. Phonon dispersion and thermodynamic properties of fluorite PuO_2

To our knowledge, no experimental phonon frequency results have been published for PuO_2 . In 2008, Yin and Savrasov [21] successfully obtained the phonon dispersions of both UO_2 and PuO_2 by employing the LDA+DMFT scheme. They found that the dispersive longitudinal optical (LO) modes do not participate much in the heat transfer due to their large anharmonicity and only longitudinal acoustic (LA) modes having large phonon group velocities are efficient heat carriers. In 2009, Minamoto *et al.* [49] investigated the thermodynamic properties of PuO_2 based on their calculated phonon dispersion within the pure GGA scheme. In present work, we have calculated the Born effective charges Z^* and dielectric constants ϵ_∞ of PuO_2 before phonon dispersion calculation due to their critical importance to correct the LO-TO splitting. For fluorite PuO_2 , the effective charge tensors for both Pu and O are isotropic because of their position symmetry. After calculation, the Born effective charges of Pu and O ions for AFM PuO_2 are found to be $Z_{\text{Pu}}^*=5.12$ and $Z_{\text{O}}^*=-2.56$, respectively, within LDA+ U formalism with the choice of $U=4.0$ eV. In addition, the macroscopic static dielectric tensor is also isotropic and our computed value of dielectric constant ϵ_∞ is 5.95 for the AFM phase. As for phonon dispersion, the Hellmann-Feynman theorem and the direct method [50] are employed to calculate the phonon curves along $\Gamma-X-K-\Gamma-L-X-W-L$ directions in the BZ, together with the phonon density

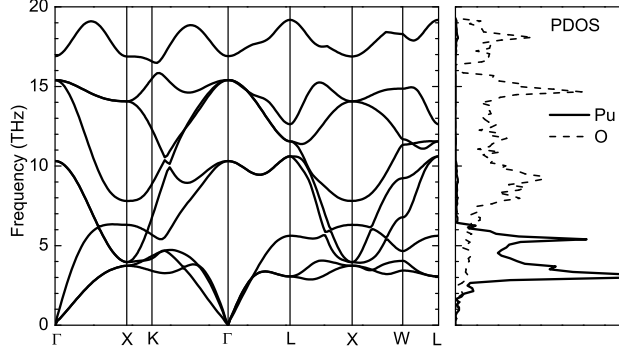


FIG. 7: Phonon dispersion curves (left panel) and corresponding PDOS (right panel) for AFM PuO₂ calculated within LDA+ U formalism with $U=4$ eV.

of states. We use $2\times 2\times 2$ fcc supercell containing 96 atoms and $3\times 3\times 3$ Monkhorst-Pack k -point mesh for the BZ integration. In order to calculate the Hellmann-Feynman forces, we displace four atoms (two Pu and two O atoms) from their equilibrium positions and the amplitude of all the displacements is 0.02 \AA .

The calculated phonon dispersion curves are displayed in Fig. 7 for the AFM phase of PuO₂. In the fluorite primitive cell, there are only three atoms (one Pu and two O atoms). Therefore, nine phonon modes exist in the dispersion relations. One can see that the LO-TO splitting at Γ point becomes evident by the inclusion of polarization effects. In addition, due to the fact that plutonium atom is heavier than oxygen atom, the vibration frequency of plutonium atom is lower than that of oxygen atom. As a consequence, the phonon density of states for PuO₂ can be viewed as two parts. One is the part lower than 6.4 THz where the main contribution comes from the plutonium sublattice, while the other part higher than 6.4 THz are dominated by the dynamics of the light oxygen atoms.

Thermodynamic properties of AFM PuO₂ calculated within LDA+ U formalism with the choice of $U=4.0$ eV are determined by phonon calculation using the quasiharmonic approximation [51], under which the Gibbs free energy $G(T,P)$ is written as

$$G(T, P) = F(T, V) + PV. \quad (17)$$

Here, $F(T, V)$ is the Helmholtz free energy at temperature T and volume V and can be expressed as

$$F(T, V) = E(V) + F_{ph}(T, V) + F_{el}(T, V), \quad (18)$$

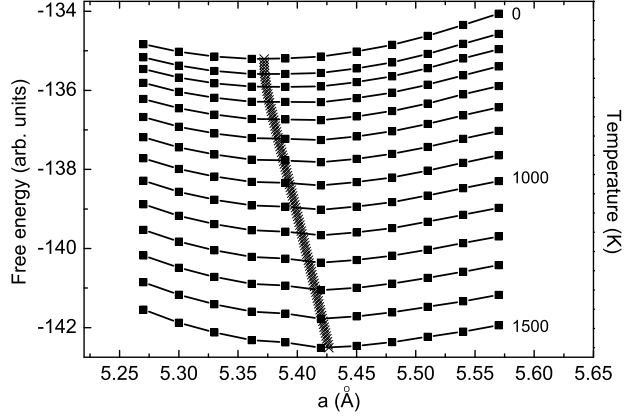


FIG. 8: Dependence of the free energy $F(T, V)$ on crystal lattice parameter a for a number of selected temperatures for AFM PuO_2 calculated within LDA+ U formalism with $U=4$ eV.

where $E(V)$ is the ground-state total energy, $F_{ph}(T, V)$ is the phonon free energy and $F_{el}(T, V)$ is the thermal electronic contribution. In present study, we focus only on the contribution of atom vibrations. The $F_{ph}(T, V)$ can be calculated by

$$F_{ph}(T, V) = k_B T \int_0^\infty g(\omega) \ln \left[2 \sinh \left(\frac{\hbar\omega}{2k_B T} \right) \right] d\omega, \quad (19)$$

where $\omega=\omega(V)$ represents the volume-dependent phonon frequencies and $g(\omega)$ is the phonon DOS.

In calculation of $F(T, V)$, the ground-state total energy and phonon free energy should be calculated by constructing several $2 \times 2 \times 2$ fcc supercells. The temperature T appears in $F(T, V)$ via the phonon term only. Calculated free energy $F(T, V)$ curves of PuO_2 for temperature ranging from 0 up to 1500 K are shown in Fig. 8. The locus of the equilibrium lattice parameters at different temperature T are also presented. The equilibrium volume $V(T)$ and the bulk modulus $B(T)$ are obtained by EOS fitting. Figure 9 shows the temperature dependence of the relative lattice parameter and the bulk modulus. Experimental results [52] are also plotted. Clearly, the lattice parameter increases approximately in the same ratio as that in experiment [52]. The bulk modulus $B(T)$ is predicted to decrease along with the increase of temperature. This kind of temperature effect is very common for compounds and metals. Besides, the specific heat at constant volume C_V can be directly calculated through

$$C_V = k_B \int_0^\infty g(\omega) \left(\frac{\hbar\omega}{k_B T} \right)^2 \frac{\exp \frac{\hbar\omega}{k_B T}}{(\exp \frac{\hbar\omega}{k_B T} - 1)^2} d\omega, \quad (20)$$

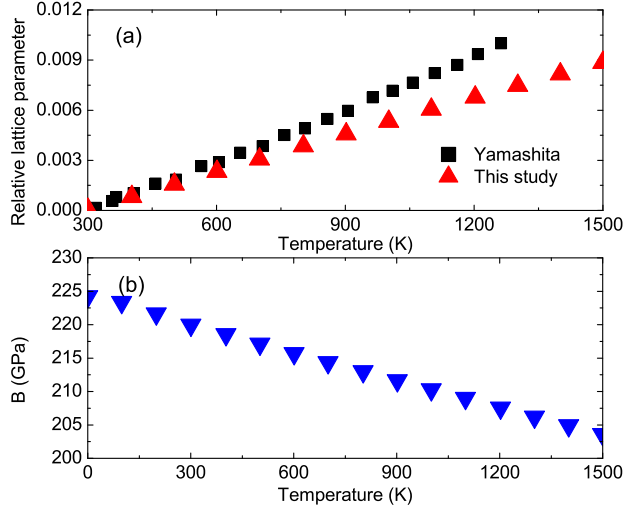


FIG. 9: (Color online) Temperature dependence of (a) relative lattice parameter $[a(T) - a(300)]/a(300)$, where $a(300)$ denotes the lattice parameter at 300 K, and (b) bulk modulus $B(T)$ of PuO_2 . Experimental results from [52] are also shown in panel (a).

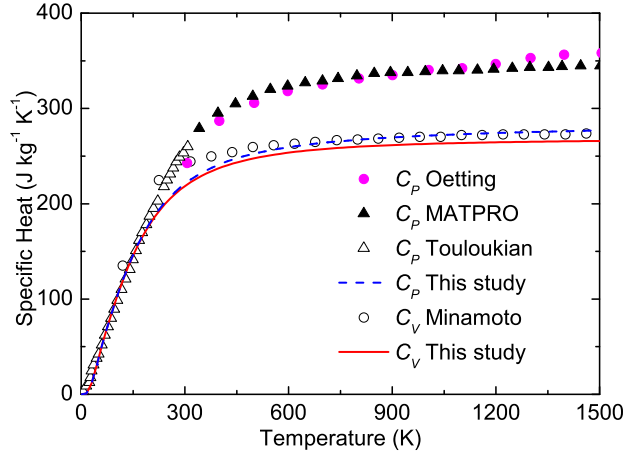


FIG. 10: (Color online) Calculated specific heat at constant pressure (C_P) and at constant volume (C_V). For comparison, previous experimental results from [49, 53–55] are also shown.

while the specific heat at constant pressure C_P can be evaluated by the thermodynamic relationship $C_P - C_V = \alpha_V^2(T)B(T)V(T)T$, where the isobaric thermal expansion coefficient can be calculated according to the formula $\alpha_V(T) = \frac{1}{V} \left(\frac{\partial V}{\partial T} \right)_P$. Calculated C_P and C_V are presented in Fig. 10. Clearly, the calculated C_V is in good agreement with experiment [49] in all investigating temperature domain, while the predicted C_P only accords well with the

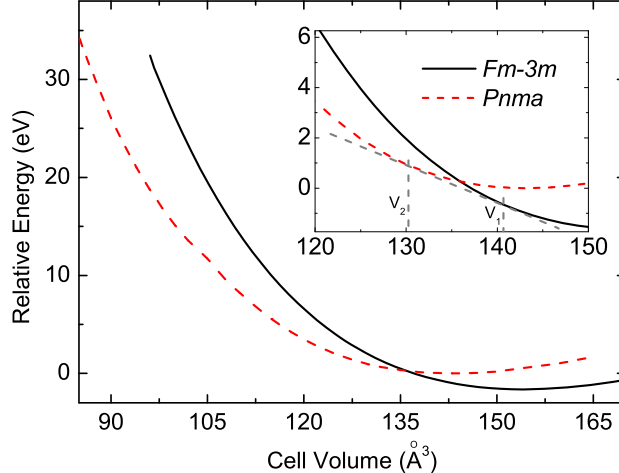


FIG. 11: (Color online) Comparison of relative energy vs the cell volume for AFM PuO_2 in $Fm\bar{3}m$ and $Pnma$ phases. The total energy of $Pnma$ phase at 0 GPa is set as zero. A phase transition at 24.3 GPa is predicted by the slope of the common tangent rule, as shown in the inset.

corresponding experimental data [53] below 300 K due to the intrinsic fact that near zero temperature C_P and C_V approach to the same value. The disagreement of C_P between theory and experiments [54, 55] in high temperature domain is believed to mainly originate from the quasiharmonic approximation we use.

D. High pressure behavior of PuO_2

In the following, we will focus our attention on the behavior of plutonium dioxide under hydrostatic compression. Two experimentally established structures, $Fm\bar{3}m$ and $Pnma$ phases, are investigated in detail. The relative energies (per unit cell) of the two phases at different volumes are calculated and shown in Fig. 11. Obviously, the $Fm\bar{3}m$ phase is stable under ambient pressure while under high pressure the $Pnma$ phase becomes stable. According to the rule of common tangent of two energy curves, a phase transition at 24.3 GPa is predicted by the slope shown in the inset of Fig. 11. Besides, we also determine the phase transition pressure by comparing the Gibbs free energy as a function of pressure. At 0 K, the Gibbs free energy is equal to enthalpy H , expressed as $H=E+PV$. The crossing between the two enthalpy curves (not shown) also gives phase transition pressure of 24.3 GPa, which is fully consistent with above result in terms of the common tangent rule. This

TABLE VII: Calculated structural parameters (in \AA), pressure (in GPa), and relative energy (in eV) with respect to the total energy at 0 GPa of the $Pnma$ PuO_2 at two constant volumes from experiment [8]. For comparison, the experimental values are also listed.

Magnetism	a	b	c	Pressure	Relative Energy
NM	6.502	3.165	6.087	82.9	32.87
FM	7.478	3.088	5.424	124.2	31.80
AFM	5.585	3.410	6.577	38.6	1.90
Expt.	5.64	3.38	6.57	39	
Expt.	5.62	3.44	6.49	49	
AFM	5.492	3.398	6.539	48.8	2.80

value is smaller by ~ 15 GPa when compared to the experiment measurement by Dancausse *et al* [8]. We notice that Li *et al* [56] predicted a transition pressure of about 45 GPa employing the full-potential linear-muffin-tin-orbital (FPLMTO) method. However, they only considered the NM and FM phases in their calculations of the $Fm\bar{3}m$ and $Pnma$ PuO_2 . No results were calculated for the AFM phase. In our present study, we first optimize the $Pnma$ PuO_2 at constant volume (about 125.2 \AA^3) of the experimental value at 39 GPa [8]. Our calculated structural parameters of the NM, FM, and AFM phases are tabulated in Table VII. Obviously, the AFM phase is the most stable phase and its structural parameters are well consistent with experiment. As seen in Table VII, results of AFM phase at 49 GPa is also consistent with experiment. Therefore, we will only consider the results of AFM phase in the following discussion. In addition, obvious discrepancy between two works [8, 41] from the same experimental group involving the transition pressure of ThO_2 was noticed in our previous study [25]. While the transition was reported firstly to start at 40 GPa [8], later, through improving experimental measurement technique, which can capture the two phases cohabitation zone during transition process, Idiri *et al* [41] observed that the transition really begins around 33 GPa. Our previous study [25] predicted that the phase transition of ThO_2 started at around 26.5 GPa. Idiri *et al* [41] also stated that the bulk modulus of PuO_2 were largely overestimated in their previous work [8]. Thus, we believe that their former report [8] also overestimated the transition pressure of PuO_2 in some degree. So the predicted transition pressure of PuO_2 , which is very close to that of ThO_2 [25], is understandable.

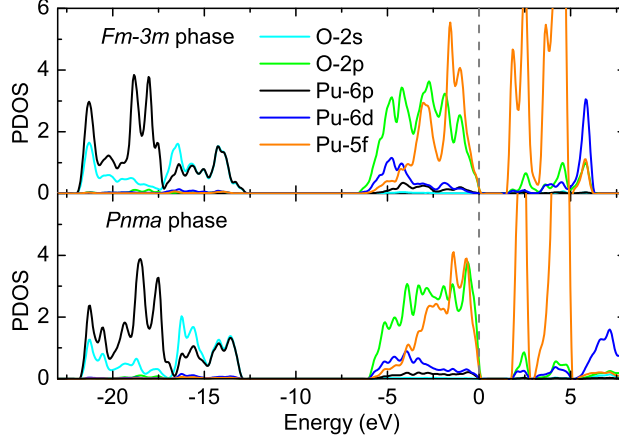


FIG. 12: (Color online) Partial density of states (PDOS) for (a) $Fm\bar{3}m$ phase and (b) $Pnma$ phase at around 25 GPa. The Fermi energy level is zero. The energy gaps of $Fm\bar{3}m$ phase and $Pnma$ phase are 1.51 eV and 1.65 eV, respectively.

Figure 12 compares the PDOS of the $Fm\bar{3}m$ and $Pnma$ phases of PuO_2 at a pressure of around 25 GPa, close to the transition pressure. One can see evident increase of the band gap from 1.51 eV in the fluorite phase to 1.65 eV in the cotunnite phase. In study of UO_2 , Geng *et al* [24] also predicted this similar behavior. However, our previous study of ThO_2 [25] found that the band gap is reduced from $Fm\bar{3}m$ phase to $Pnma$ phase. The reason is simply that ThO_2 is a charge-transfer insulator, while PuO_2 and UO_2 are the Mott-type insulators. From Fig 12, one can see that while O $2s$ and Pu $6p$ states expand in the low bands, O $2p$ and Pu $5f/6d$ states are mainly featured near the Fermi level and have prominent hybridization characters in a width of 6.3 (5.9) eV for $Fm\bar{3}m$ ($Pnma$) phase. There is no evident difference between the two phases in their $5f$ electronic localization behavior. Therefore, our study of PuO_2 supports our previous [25] viewpoint: the phenomenon of volume collapse during high-pressure phase transition of the actinide dioxides is mainly attributed to the ionic (instead of electronic) response to the external compression.

The relative volume V/V_0 evolution with pressure for PuO_2 in both $Fm\bar{3}m$ and $Pnma$ phases are shown in Fig 13. For comparison, the experimental [8] data are also shown in the figure. Clearly, our calculated P-V equation of state is well consistent with the experimental measurement for the two phases of PuO_2 . Specially, at the calculated transition pressure (24.3 GPa), our result in Fig. 13 gives that the volume collapse upon phase transition is

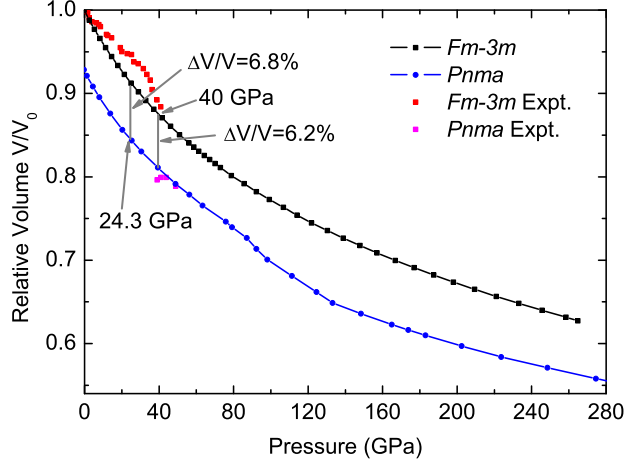


FIG. 13: (Color online) Calculated compression curves of PuO_2 compared with experimental measurements. The volume collapses at our predicted phase transition point 24.3 GPa and experimental [8] phase transition pressure 40 GPa are labeled.

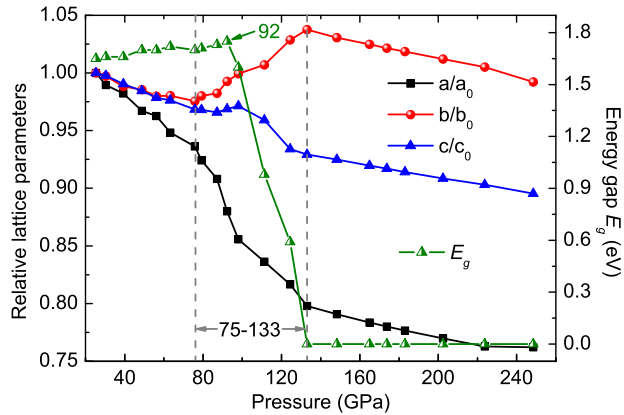


FIG. 14: (Color online) Pressure behavior of the relative lattice parameters of the $Pnma$ phase, where the drastic change in the relative lattice constants (region between dashed lines) indicates an isostructural transition. Besides, the pressure behavior of the insulating band gap is also shown.

6.8%. This value is evidently underestimated compared with the experimental data of 12% [8]. The discrepancy between experiment and our calculation needs more experimental and theoretical works to examine. After phase transition, we also find an isostructural transition occurring between 75 and 133 GPa for the $Pnma$ phase. This isostructural transition of actinide dioxides was first found in DFT calculations of UO_2 by Geng *et al* [24] and then

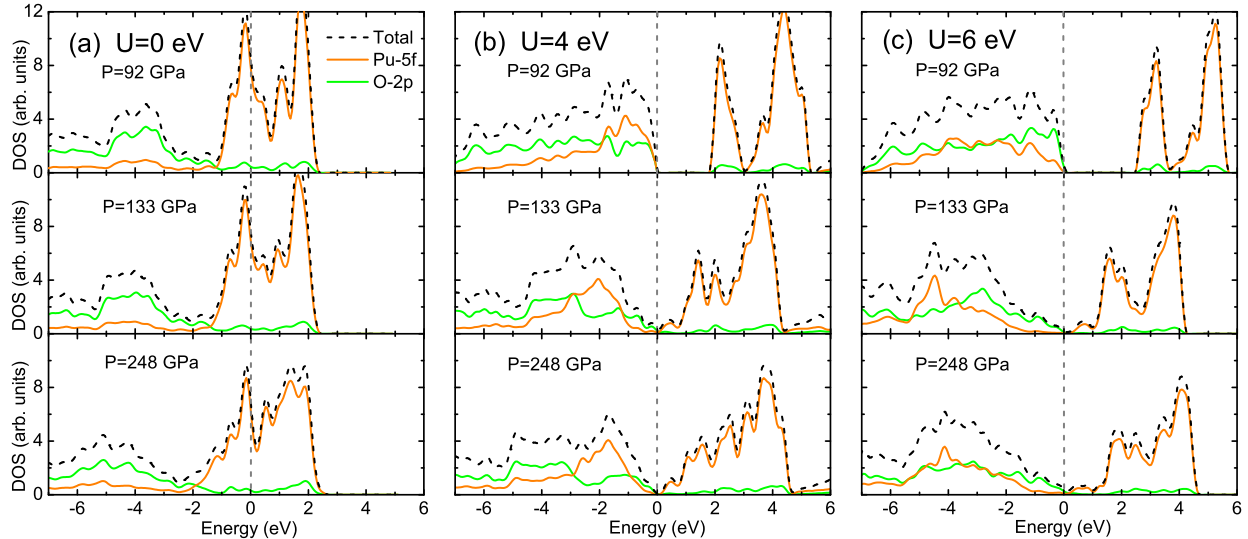


FIG. 15: (Color online) The total DOS for the cotunnite PuO_2 AFM phase calculated at selected pressures within LDA+ U formalism with (a) $U=0$ eV, (b) $U=4$ eV, and (c) $U=6$ eV. The projected DOSs for the Pu $5f$ and O $2p$ orbitals are also shown. The Fermi energy level is set at zero.

observed in study of ThO_2 [25]. The pressure dependence of the three lattice parameters (with respect to their values at calculated transition pressure 24.3 GPa) for the $Pnma$ phase of PuO_2 are plotted in Fig. 14. Similar to the studies of UO_2 and ThO_2 [24, 25], in pressure region before 75 GPa, the responses of the three relative lattice parameters to the compression are anisotropic in the sense that the compression of the middle axis a is most rapid compared to those of the long axis c and small axis b , which vary upon compression almost in the same tendency. When the pressure becomes higher to be between 75 and 133 GPa, remarkably, it reveals in Fig. 14 that all the three relative lattice parameters undergo dramatic variations by the fact that the small axis b has a strong rebound and the middle a is collapsed. When the pressure is beyond 133 GPa, then the variations of the three relative lattice parameters become smooth and approach isotropic compression. This signifies a typical isostructural transition for the $Pnma$ phase of PuO_2 .

Moreover, we also present in Fig. 14 the evolution of the insulating band gap with pressure for $Pnma$ phase of PuO_2 . Apparently, the band gap behaves smooth in pressure region of 25-92 GPa, then turns to decrease suddenly from about 1.75 eV to zero under compression from 92 to 133 GPa. This clearly indicates that the $Pnma$ phase will occur a metallic transition after external pressure exceeds 133 GPa. As Fig. 15(b) shows, with

increasing pressure in the crossover range between 92 and 133 GPa, the $5f$ electrons in the cotunnite phase of PuO_2 are more delocalized and the $5f$ bands are largely broadened. As a result, the Mott-type band gap is narrowed and even blurred, which is characterized by finite occupancies of O $2p$ and Pu $5f$ orbitals at the Fermi level, by the increasing kinetic energy of $5f$ electrons. In order to see the pressure behavior of electronic structure with different values of Hubbard parameter U for cotunnite PuO_2 , we have plotted in Fig. 15 the total DOS and PDOS for the cotunnite PuO_2 AFM phase calculated at 92, 133, and 248 GPa within LDA+ U formalism with $U=0, 4, \text{ and } 6$ eV. It clearly shows that (i) the pure LDA always produces incorrect electronic structure in the full pressure region we considered, and (ii) it is not imperative to adjust U as varying pressure by the fact revealed in Figs. 15(b) and 15(c) that the electronic properties and insulator-metal transition behavior at high pressures show the similar character for the two choices of Hubbard parameter $U=4$ eV and $U=6$ eV. Based on this observation, in the above high-pressure calculations we have fixed the value of U to be 4 eV. It should be stressed that the metallic transition is not unique for PuO_2 . Similar phenomenon has also been observed in other actinide dioxides [24]. Besides, the variation of the local magnetic moment of plutonium atoms is almost same for $Fm\bar{3}m$ and $Pnma$ phases, implying that the magnetic property is insensitive to the structure transition in PuO_2 . Actually, the calculated amplitude of local spin moment varies from ~ 4.1 to $\sim 3.8 \mu_B$ (per Pu atom) for both fluorite and cotunnite phases in pressure range from 0 to 255 GPa. No paramagnetic transition for this material has been observed in present study.

IV. CONCLUSIONS

In conclusion, the ground state properties as well as the high pressure behavior of PuO_2 were studied by means of the first-principles DFT+ U method. By choosing the Hubbard U parameter around 4 eV within the LDA+ U approach, the electronic structure, lattice parameters, and bulk modulus were calculated for both the ambient $Fm\bar{3}m$ and the high-pressure $Pnma$ phases of PuO_2 and were shown to accord well with experiments. Results for UO_2 were also presented for comparison. Based on these results, the Pu–O and U–O bonds were interpreted as displaying a mixed ionic/covalent character by electronic structure analysis. After comparing with our previous calculations of NpO_2 and ThO_2 , we demonstrated

that the Pu–O, U–O, and Np–O bonds have stronger covalency than the Th–O bond. The ionicity of Th–O bond was found to be the largest among these four kinds of actinide dioxides. In addition, the stability of the two phases at zero pressure was predicted through calculating elastic constants and phonon dispersion. The hardness, Debye temperature, ideal tensile strength, and thermodynamic properties were calculated and analyzed to support the practical application of PuO₂. We showed that the hardness of $Fm\bar{3}m$ phase is ~ 27 GPa and the Debye temperatures of $Fm\bar{3}m$ and $Pnma$ phases are 354.5 and 350.0 K, respectively. For $Fm\bar{3}m$ PuO₂, the ideal tensile strengths are calculated within FPCTT to be 81.2, 28.3, and 16.8 GPa in tensile deformations along the [100], [110], and [111] directions, respectively. The volume thermal expansion and specific heat at constant volume curves are well consistent with available experiments. However, the discrepancy between measured and our calculated specific heat at constant pressure in high temperature domain is evident. This needs further theoretical work by including the anharmonic ionic contribution to decrease this kind of discrepancy.

In studying the pressure behavior of PuO₂, we showed that the $Fm\bar{3}m \rightarrow Pnma$ transition occurs at 24.3 GPa. Although this value is large smaller than the experimental report, we believe that our calculated result is reasonable. One reason is that the lattice parameters of $Pnma$ PuO₂ AFM phase calculated at around 39 and 49 GPa are precisely consistent with experiment. Another is the fact that the experiment needs improvement as having been indicated in study of UO₂ and ThO₂ [41]. Furthermore, we extended the pressure up to 280 GPa for the two structures of PuO₂. A metallic transition at around 133 GPa and an isostructural transition in pressure range of 75-133 GPa were predicted for the $Pnma$ phase. Also, the calculated amplitude of local spin moment only varies from ~ 4.1 to $\sim 3.8 \mu_B$ (per Pu atom) for both fluorite and cotunnite phases in pressure range from 0 to 255 GPa. No paramagnetic transition for this material has been observed.

Acknowledgments

We gratefully thank G. H. Lu, H. B. Zhou, and X. C. Li for illustrating discussion on FPCTT. This work was supported by the Foundations for Development of Science and

- [1] S. Heathman *et al.*, *Science* **309**, 110 (2005).
- [2] I. D. Prodan, G. E. Scuseria, and R. L. Martin, *Phys. Rev. B* **76**, 033101 (2007).
- [3] R. Atta-Fynn and A. K. Ray, *Phys. Rev. B* **76**, 115101 (2007).
- [4] K. T. Moore and G. van der Laan, *Rev. Mod. Phys.* **81**, 235 (2009).
- [5] J. M. Haschke, T. H. Allen, and L. A. Morales, *Science* **287**, 285 (2000).
- [6] M. Butterfield, T. Durakiewicz, E. Guziewicz, J. Joyce, A. Arko, K. Graham, D. Moore, and L. Morales, *Surf. Sci.* **571**, 74 (2004).
- [7] T. Gouder, A. Seibert, L. Havela, and J. Rebizant, *Surf. Sci.* **601**, L77 (2007).
- [8] J. P. Dancausse, E. Gering, S. Heathman, and U. Benedict, *High Press. Res.* **2**, 381 (1990).
- [9] C. E. Boettger and A. K. Ray, *Int. J. Quantum Chem.* **90**, 1470 (2002).
- [10] C. McNeilly, *J. Nucl. Mater.* **11**, 53 (1964).
- [11] S. L. Dudarev, D. N. Manh, and A. P. Sutton, *Philos. Mag. B* **75**, 613 (1997).
- [12] S. L. Dudarev, G. A. Botton, S. Y. Savrasov, C. J. Humphreys, and A. P. Sutton, *Phys. Rev. B* **57**, 1505 (1998).
- [13] S. L. Dudarev, M. R. Castell, G. A. Botton, S. Y. Savrasov, C. Muggelberg, G. A. D. Briggs, A. P. Sutton, and D. T. Goddard, *Micron* **31**, 363 (2000).
- [14] I. D. Prodan, G. E. Scuseria, J. A. Sordo, K. N. Kudin, and R. L. Martin, *J. Chem. Phys.* **123**, 014703 (2005).
- [15] L. Petit, A. Svane, Z. Szotek, W. M. Temmerman, and G. M. Stocks, *Phys. Rev. B* **81**, 045108 (2010).
- [16] B. Sun, P. Zhang, and X.-G. Zhao, *J. Chem. Phys.* **128**, 084705 (2008).
- [17] B. Sun and P. Zhang, *Chin. Phys. B* **17**, 1364 (2008).
- [18] D. A. Andersson, J. Lezama, B. P. Uberuaga, C. Deo, and S. D. Conradson, *Phys. Rev. B* **79**, 024110 (2009).
- [19] G. Jomard, B. Amadon, F. Bottin, and M. Torrent, *Phys. Rev. B* **78**, 075125 (2008).
- [20] H. Shi, M. Chu, and P. Zhang, *J. Nucl. Mater.* **400**, 151 (2010).
- [21] Q. Yin and S. Y. Savrasov, *Phys. Rev. Lett.* **100**, 225504 (2008).
- [22] R. F. W. Bader, *Atoms in Molecules: A Quantum Theory* (Oxford University Press, New

- York, 1990).
- [23] W. Tang, E. Sanville, and G. Henkelman, *J. Phys.: Condens. Matter* **21**, 084204 (2009).
 - [24] H. Y. Geng, Y. Chen, Y. Kaneta, and M. Kinoshita, *Phys. Rev. B* **75**, 054111 (2007).
 - [25] B. T. Wang, H. Shi, W. D. Li, and P. Zhang, *J. Nucl. Mater.* **399**, 181 (2010).
 - [26] P. E. Blöchl, *Phys. Rev. B* **50**, 17953 (1994).
 - [27] G. Kresse and J. Furthmüller, *Phys. Rev. B* **54**, 11169 (1996).
 - [28] W. Kohn, L. J. Sham, *Phys. Rev.* **140** (1965) A1133.
 - [29] J. P. Perdew, K. Burke, and Y. Wang, *Phys. Rev. B* **54**, 16533 (1996).
 - [30] H. J. Monkhorst and J. D. Pack, *Phys. Rev. B* **13**, 5188 (1972).
 - [31] S. L. Dudarev, D. N. Manh, and A. P. Sutton, *Philos. Mag. B* **75**, 613 (1997).
 - [32] B. T. Wang, H. Shi, W. D. Li, and P. Zhang, *Phys. Rev. B* **81**, 045119 (2010).
 - [33] C. E. Boettger and A. K. Ray, *Int. J. Quantum Chem.* **80**, 824 (2000).
 - [34] I. D. Prodan, G. E. Scuseria, and R. L. Martin, *Phys. Rev. B* **73**, 045104 (2006).
 - [35] F. Birch, *Phys. Rev.* **71**, 809 (1947).
 - [36] J. F. Nye, *Physical Properties of Crystals* (Oxford University Press, Oxford, 1985).
 - [37] R. Hill, *Phys. Phys. Soc. London* **65**, 349 (1952).
 - [38] J. Hanies, J. M. Leger, and G. Bocquillon, *Annu. Rev. Mater. Res.* **31**, 1 (2001).
 - [39] J. P. Watt, *J. Appl. Phys.* **50**, 6290 (1979).
 - [40] P. Ravindran, L. Fast, P.A. Korzhavyi, B. Johansson, J. Wills, O. Eriksson, *J. Appl. Phys.* **84**, 4891 (1998)
 - [41] M. Idiri, T. Le Bihan, S. Heathman, and J. Rebizant, *Phys. Rev. B* **70**, 014113 (2004).
 - [42] S. C. Abrahams and F. S. L. Hsu, *J. Chem. Phys.* **63**, 1162 (1975).
 - [43] R. B. Kaner, J. J. Gilman, and S. H. Tolbert, *Science* **308**, 1268 (2005).
 - [44] A. Simunek and J. Vackar, *Phys. Rev. Lett.* **96**, 085501 (2006).
 - [45] A. Simunek, *Phys. Rev. B* **75**, 172108 (2007).
 - [46] F. Gao, J. He, E. Wu, S. Liu, D. Yu, D. Li, S. Zhang, and Y. Tian, *Phys. Rev. Lett.* **91**, 015502 (2003).
 - [47] Y. Zhang, G. H. Lu, S. H. Deng, T. M. Wang, H. B. Xu, M. Kohyama, and R. Yamamoto, *Phys. Rev. B* **75**, 174101 (2007).
 - [48] O. H. Nielsen and R. M. Martin, *Phys. Rev. B* **32**, 3780 (1987).
 - [49] S. Minamoto, M. Kato, K. Konashi, and Y. Kawazoe, *J. Nucl. Mater.* **385**, 18 (2009).

- [50] K. Parlinski, Z.-Q. Li, and Y. Kawazoe, Phys. Rev. Lett. **78**, 4063 (1997).
- [51] A. Siegel, K. Parlinski, and U. D. Wdowik, Phys. Rev. B **74**, 104116 (2006).
- [52] T. Yamashita, N. Nitani, T. Tsuji, and H. Inagaki, J. Nucl. Mater. **247**, 90 (1997).
- [53] Y. S. Touloukian, R. K. Kirby, R. E. Taylor, T. Y. R. Lee, *Thermal Expansion-nonmetallic Solids*, The TRPC DATA Series, Vol. 13 (Plenum, New York, 1977).
- [54] F. L. Oetting, J. Nucl. Mater. **105**, 257 (1982).
- [55] MATPRO-A *Library of Materials Properties for Light-Water-Reactor Accident Analysis* in: SCDAP/RELAP5/MOD3.1 Code Manual, Vol IV, NUREG/CR-6150 EGG-2720 (INEL, USA, 1993).
- [56] S. Li, R. Ahuja, and B. Johansson, High Press. Res. **22**, 471 (2002).